

Particle dynamics in a non-flaring solar active region

J. Threlfall¹, Ph.-A. Bourdin², T. Neukirch¹, and C. E. Parnell¹

¹ School of Mathematics and Statistics, University of St Andrews, St Andrews, Fife, KY16 9SS, U.K. e-mail: {jwt9;tn3;cep}@st-andrews.ac.uk

² Space Research Institute, Austrian Academy of Sciences, Schmiedlstr. 6, 8042 Graz, Austria e-mail: Philippe.Bourdin@oeaw.ac.at

ABSTRACT

Aims. The aim of this work is to investigate and characterise particle behaviour in a (observationally-driven) 3D MHD model of the solar atmosphere above a slowly evolving, non-flaring active region.

Methods. We use a relativistic guiding-centre particle code to investigate particle acceleration in a single snapshot of the 3D MHD simulation.

Results. Despite the lack of flare-like behaviour in the active region, direct acceleration of electrons and protons to non-thermal energies ($\lesssim 420$ MeV) was found, yielding spectra with high-energy tails which conform to a power law. Examples of particle dynamics, including particle trapping caused by local electric rather than magnetic field effects, are observed and discussed, together with implications for future experiments which simulate non-flaring active region heating and reconnection.

Key words. Plasmas - Sun: corona - Sun: magnetic fields - Sun: activity - Acceleration of particles

1. Introduction

Understanding the dynamics of charged particles in reconnecting solar processes, in particular the acceleration of particles in solar flares, is of fundamental importance for advancing our knowledge of plasma behaviour in general (for example, recent reviews on particle acceleration in flares include Vilmer et al. 2011; Fletcher et al. 2011; Zharkova et al. 2011; Cargill et al. 2012). There has been growing observational evidence that accelerated particle populations also occur in smaller scale processes such as micro-flares (see e.g. Hannah et al. 2011, and references therein) or nano-flares (Testa et al. 2014); these processes are also often associated with magnetic reconnection.

In the context of the solar atmosphere, it is now widely accepted that magnetic reconnection contributes to the maintenance of thermal (contributing to coronal heating as discussed in Parnell & De Moortel 2012; Parnell et al. 2015) and sporadic generation of non-thermal (high-energy) particle populations. Since magnetic reconnection is intrinsically associated with field aligned electric fields (e.g. Schindler et al. 1988; Hesse & Schindler 1988; Schindler et al. 1991) and these electric fields are well known accelerators of charged particles, the question of how the local particle dynamics on all scales are affected by reconnection electric fields remains open and important. Additionally, magnetic reconnection can lead to rapid magnetic field changes that can also cause particle acceleration, such as collapsing magnetic traps (e.g. Grady & Neukirch 2009; Grady et al.

2012; Eradat Oskoui et al. 2014; Eradat Oskoui & Neukirch 2014).

Previous studies of particle behaviour typically use a test particle approach to study a wide variety of configurations, all of which are underpinned by or directly investigate magnetic reconnection. For instance, the acceleration of particles at specific topological features has been explored in studies at/near 2/2.5D null points (e.g. Bulanov & Sasorov 1976; Bruhwiler & Zweibel 1992; Kliem 1994; Litvinenko 1996; Browning & Vekstein 2001; Zharkova & Gordovskyy 2004, 2005; Wood & Neukirch 2005; Hannah & Fletcher 2006; Drake et al. 2006) and, more recently, 3D null points (e.g. Dalla & Browning 2005, 2006, 2008; Guo et al. 2010; Stanier et al. 2012), stressed magnetic fields/current sheets (e.g. Turkmani et al. 2005; Onofri et al. 2006; Gordovskyy et al. 2010) and 3D magnetic separators (Threlfall et al. 2015). Acceleration in more complex 3D models such as twisted coronal loops (Gordovskyy & Browning 2011; Gordovskyy et al. 2014) have also been investigated. A significant step forward from the analysis of a localised reconnection site was taken by Baumann et al. (2013), who combined localised particle-in-cell (PIC) analysis in the vicinity of a reconnecting null-point with a magnetohydrodynamic (MHD) model of the surrounding active region (AR). This allowed the global impact sites of the particles to be identified.

Instead of considering an isolated reconnection process, whether embedded in a global field or not, we take a different approach and investigate the particle acceleration in an observa-

tionally driven MHD simulation of an AR. A decade ago, the first MHD simulations of downscaled ARs were produced that were based on extrapolated observed magnetograms, driven in a manner which approximated motions arising from convection cells on a range of scales (e.g. [Gudiksen & Nordlund 2005b,a](#)). Only recently have large-scale computations been performed that model a full AR without downscaling ([Bourdin et al. 2013](#)).

The MHD simulation we will use was designed to model the coronal response to photospheric driving by advection of field-lines due to horizontal granular motions in the photosphere, where the plasma beta is larger than one ([Bourdin et al. 2013](#)). The base of the simulation is prescribed by an observed AR magnetogram with the subsequent field-line braiding inducing currents in the corona due to quasi-static changes propagating at the Alfvén speed along the field into the corona. In effect, this is one implementation of the field-line braiding mechanism of [Parker \(1972\)](#) and results in coronal loops with temperatures of around 1.5 MK. The location, apex height, and plasma flows along these loops all broadly match observations ([Bourdin et al. 2013](#)). The feasibility of this field-line braiding mechanism to heat the corona sufficiently by Ohmic dissipation of induced currents is demonstrated in [Bourdin et al. \(2015\)](#). This suggests that reconnection occurs regularly throughout the AR, and, hence, there must be widespread parallel electric fields.

In this paper, we investigate what, if any, particle acceleration occurs in this MHD simulation of an observed non-flaring AR ([Bourdin et al. 2013](#)). In such a model there are a wide range of locations (magnetic configurations) at which reconnection occurs, as well as a range of different reconnection regimes in operation. Thus, the MHD model we investigate here incorporates many of the particle acceleration scenarios considered in isolation mentioned above. Thus, in this paper we consider the electromagnetic fields generated in a non-flaring active-region simulation based on observations and determine the effects they have on charged particle dynamics.

The primary objective of the present work is to survey the particle dynamics which result from MHD simulations of a non-flaring AR, and to determine the extent and locations to which particles may be accelerated by such a model. The paper is organised as follows: in Sect. 2 we discuss the model itself, introducing both the MHD simulation domain (described in Sect. 2.1) and the equations which govern test particle motion (in Sect. 2.2). A survey of orbit behaviour throughout the AR core is outlined and discussed in Sect. 3, before examining specific test particle examples in detail in Sect. 4. A discussion of our findings is presented in Sect. 5 before conclusions and future areas of study are outlined in Sect. 6.

2. Model setup

Our model can be broadly split into two parts: a time-dependent MHD simulation (modelling the solar corona above an AR) on time-scales of hours into which we insert particles (using a sin-

gle evolved snapshot), and the test particle motion itself on time scales of seconds. A brief overview of both parts are described in the following sections:

2.1. MHD active region model

The AR MHD simulation of [Bourdin et al. \(2013\)](#) that we use is observationally driven; a potential-field extrapolation from an observed line-of-sight magnetogram on the base determines the initial magnetic state within the numerical domain. This magnetogram was obtained from the Hinode solar observatory ([Kosugi et al. 2007](#); [Culhane et al. 2007](#); [Golub et al. 2007](#)). The region in question is located close to the centre of the solar disk on the 14th November 2007; while not assigned an NOAA AR number, the observed region displayed many typical AR characteristics (for example, a system of closed loop structures, visible in both EUV and X-ray wavelengths, linking a pair of strong magnetic field patches of opposite polarity; see Fig. 1).

While data from the Reuven Ramaty High Energy Solar Spectroscopic Imager (RHESSI, [Lin et al. 2002](#)) was unavailable for this date, the Geostationary Operational Environmental Satellite (GOES) X-ray data suggests that solar activity at this time was particularly low. The largest GOES event on the 14th November (and indeed for the preceding fortnight) was an A1-class event, while the emergence of a second AR (NOAA 10974) coincided with a B1-class event on the 17th November. From the available data, we characterise the chosen region as a relatively isolated, stable, and slowly evolving AR which (crucially) does not produce a flare within one day before and two days after the observation. Hence, it was an ideal choice for the original aim of the simulation, namely to study coronal heating.

The computational domain is periodic in the horizontal directions. In order to sufficiently isolate the main AR polarities from their periodic images, the AR observation is surrounded by a region of quiet Sun. The full horizontal extent of $235 \times 235 \text{ Mm}^2$ is covered by 1024^2 grid points; approximately a quarter of this area covers the AR core (see Fig. 1, which shows this core region alone). Thus the grid cells in the xy directions are square with lengths of 230 km on either side.

The initial model atmosphere contains vertical stratification and is initialised smoothly to avoid spurious oscillations ([Bourdin et al. 2014b](#)). Thus the domain has a stretched grid in the vertical direction that reaches up to 156 Mm above the photosphere. The vertical extent of each cell covers between 100 km, near the photosphere, up to a maximum of 800 km in the corona. For the top boundary, we use a potential-field extrapolation to allow closed and "open" field lines to relax into a force-free state.

The compressible resistive MHD simulation was performed using the Pencil Code ([Brandenburg & Dobler 2002](#)) and incorporates gravity, viscosity, and an isotropic magnetic diffusivity $\eta = 10^{10} \text{ m}^2/\text{s}$ (more detail may be found in [Bourdin et al. 2013](#)). The initial magnetic field is evolved according to the advection of photospheric field-lines caused by a driver on the base

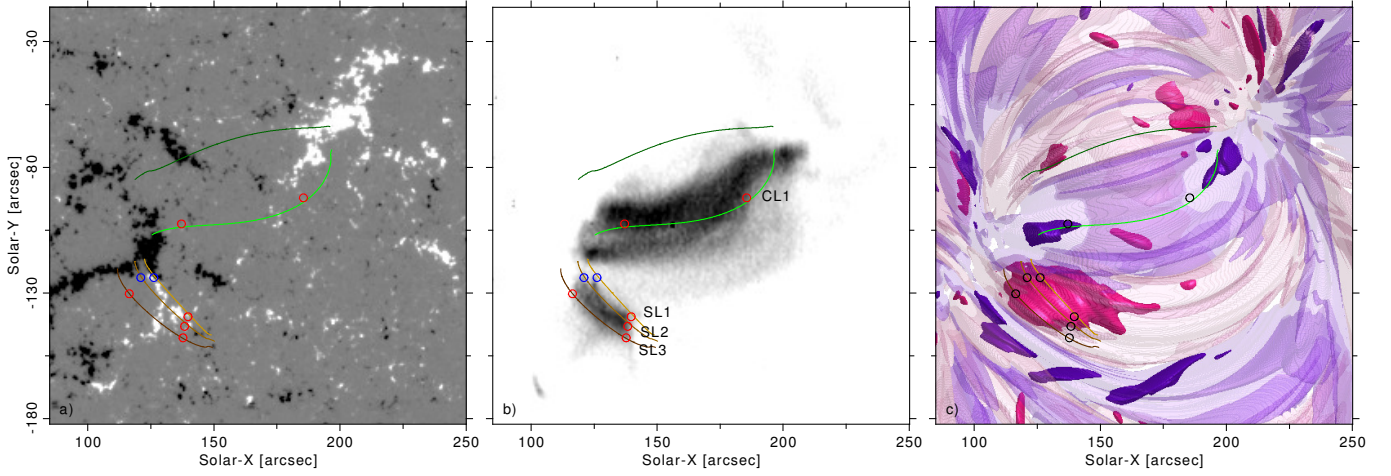


Fig. 1: Panels, from L-R, showing a) a Hinode/SOT magnetogram of an AR core seen on the 14th Nov 2007 saturated at ± 300 G, b) a Hinode/EIS image of the Fe xv emission (at 1.5 MK) of the corona above this region and c) the co-spatial and co-temporal simulated parallel electric field strength and orientation within this region (where pink/purple represents positive/negative E_{\parallel} , and the opacity represents the relative strength of E_{\parallel} - fully opaque regions contain $E_{\parallel} \in [1\%, 25\%]$ while transparent regions show $E_{\parallel} \in [0.01\%, 1\%]$ of the peak E_{\parallel} in the corona, $\sim 3.5 \text{ Vm}^{-1}$). The right hand panel is generated by simulations described in Bourdin et al. (2013), which also describes field lines which cross the intensity maxima of several EUV-emissive coronal loops, which have been overlaid in each panel; "CL" indicates core loops, while "SL" indicates shorter loops. The circles indicate EUV-emissive loop footpoints in the model and the corresponding plasma motion (and observed Doppler shifts) at these locations; red represents draining (i.e. motion along the line-of-sight away from an observer) while blue represents upflows (motion towards an observer).

which simulates horizontal granular motions in the photosphere. In this region the plasma beta is larger than one, but falls off as the density falls, such that the plasma beta is less than one in the corona. During the simulation run the magnetic field evolves self-consistently according to compressible resistive MHD, and subject to an energy equation that incorporates both heat conduction and radiative losses.

In particular, the energy input in the model is due to the Poynting flux across the base, which provides approximately $10^7 \text{ ergs}^{-1} \text{ cm}^{-2}$ (vertical signed flux average) that passes through the transition-region layer and reaches the corona. This balances the expected coronal energy requirement of an AR core region by (partial) conversion of magnetic energy into heat, which forms EUV-emissive coronal loops (Bourdin et al. 2014a). A Spitzer-type heat conduction term is included in the energy equation to model energy losses in the corona due to fast electrons (Spitzer 1962). In addition, X-ray and EUV emission is implemented through a radiative loss function which is parametrised by the local plasma density and temperature (Cook et al. 1989).

An image highlighting the distribution of parallel electric field (itself a proxy for strong parallel current) in the simulation domain can be seen in Fig. 1. The lack of flaring activity and the reported agreement with observations makes this simulation an ideal candidate to study the balance between thermal and non-thermal particle populations caused by local particle acceleration.

2.2. Relativistic particle dynamics

Having established the global environment which we will study, all that remains is to outline the equations which will govern particle behaviour. Despite the lack of flaring activity, we anticipate particle velocities may achieve values of a significant fraction of the speed of light (c). We therefore make use of the full relativistic set of guiding-centre-motion equations, outlined in Northrop (1963) (based on the treatment of Vandervoort 1960), presented here in normalised form:

$$\frac{du_{\parallel}}{dt} = \frac{d}{dt}(\gamma v_{\parallel}) = \gamma \mathbf{u}_E \cdot \frac{d\mathbf{b}}{dt} + \Omega_{scl} t_{scl} E_{\parallel} - \frac{\mu_r}{\gamma} \frac{\partial B}{\partial s}, \quad (1a)$$

$$\dot{\mathbf{R}}_{\perp} = \mathbf{u}_E + \frac{\mathbf{b}}{B^{**}} \times \left\{ \frac{1}{\Omega_{scl} t_{scl}} \left[\frac{\mu_r}{\gamma} \left(\nabla B^{*} + \frac{v_{scl}^2}{c^2} \mathbf{u}_E \frac{\partial B^{*}}{\partial t} \right) + u_{\parallel} \frac{d\mathbf{b}}{dt} + \gamma \frac{d\mathbf{u}_E}{dt} \right] + \frac{v_{scl}^2}{c^2} \frac{u_{\parallel}}{\gamma} E_{\parallel} \mathbf{u}_E \right\}, \quad (1b)$$

$$\frac{d\gamma}{dt} = \frac{v_{scl}^2}{c^2} \left[\Omega_{scl} t_{scl} \left(\dot{\mathbf{R}}_{\perp} + \frac{u_{\parallel}}{\gamma} \mathbf{b} \right) \cdot \mathbf{E} + \frac{\mu_r}{\gamma} \frac{\partial B^{*}}{\partial t} \right], \quad (1c)$$

$$\mu_r = \frac{\gamma^2 v_{\perp}^2}{B}. \quad (1d)$$

Here μ_r is the relativistic magnetic moment, for a particle with rest-mass m_0 and charge q , whose guiding centre is located at \mathbf{R} , subject to an electric field \mathbf{E} and a magnetic field \mathbf{B} (with magnitude $B(=|\mathbf{B}|)$ and unit vector $\mathbf{b}(= \mathbf{B}/B)$). Local conditions will dictate aspects of the orbit behaviour, particularly through guiding centre drifts; the largest in magnitude is typically the $\mathbf{E} \times \mathbf{B}$ drift, which has a velocity $\mathbf{u}_E(= \mathbf{E} \times \mathbf{b}/B)$. The component of velocity parallel to the magnetic field is $v_{\parallel}(= \mathbf{b} \cdot \dot{\mathbf{R}})$, while $E_{\parallel}(= \mathbf{b} \cdot \mathbf{E})$ is the magnitude of the electric field parallel to the

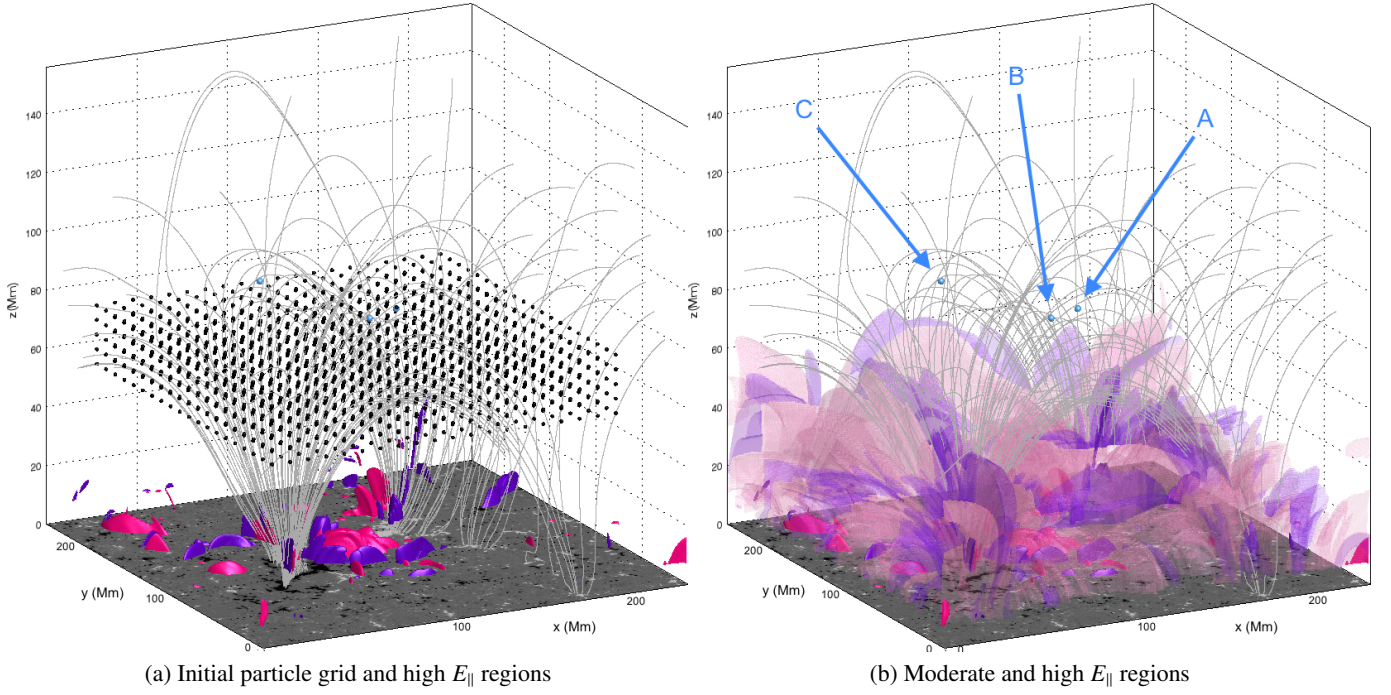


Fig. 2: Illustration of initial particle grid and electric/magnetic environment in our study. (a) shows the grid of initial particle positions (shown as black orbs) located in the coronal region of MHD simulations of a stable AR (Bourdin et al. 2013). Both (a) & (b) show interpolated magnetic field lines (grey lines) and the vector magnetogram at the base of the simulations, and isosurfaces of parallel electric field E_{\parallel} ; (a) shows opaque pink/purple surfaces of positive/negative $E_{\parallel} \in [1\%, 25\%]$ of the peak value of E_{\parallel} in the corona, while (b) also includes transparent surfaces of $E_{\parallel} \in [0.01\%, 1\%]$ of the coronal peak value ($\sim 3.5 \text{ Vm}^{-1}$). For reference, three blue orbs labelled "A", "B" and "C" indicate the initial positions of orbits studied in detail in Section. 4.

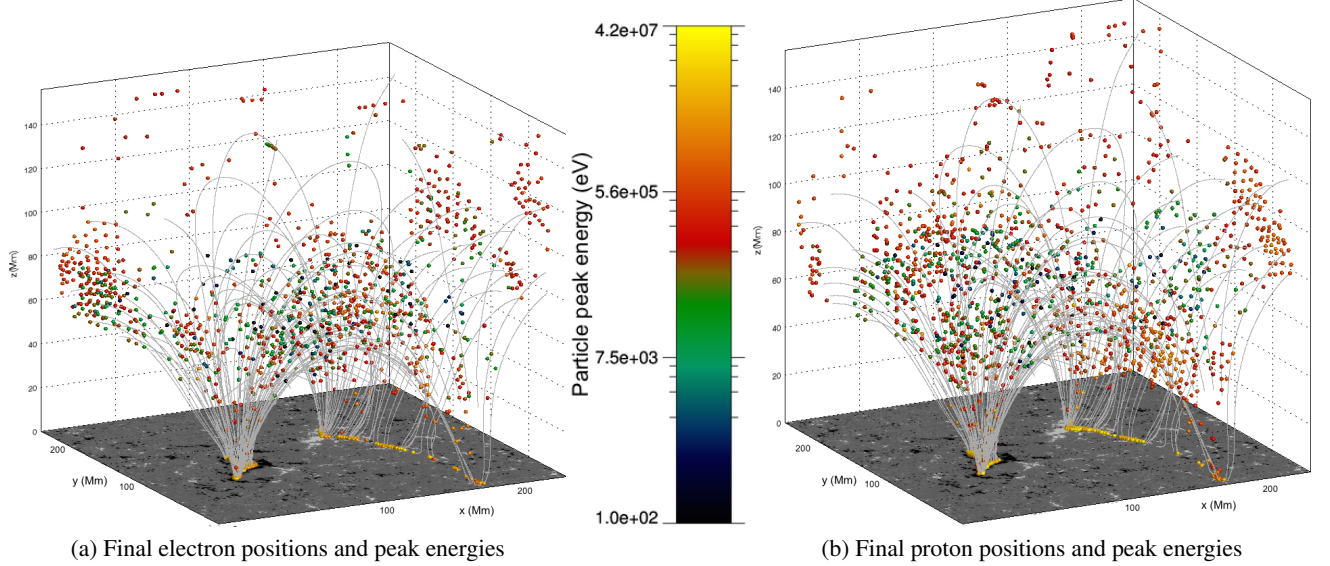


Fig. 3: Survey of the behaviour of 2000 (a) electron and (b) proton orbits, for initial position grid seen in Fig. 2a. Final particle positions are colour-coded by peak energy achieved during the orbit calculation lasting 10s (or upon leaving the MHD simulation domain) with interpolated magnetic field lines (thin grey lines) included for reference.

local magnetic field, $\dot{\mathbf{R}}_{\perp} (= \dot{\mathbf{R}} - v_{\parallel} \mathbf{b})$ is the component of velocity perpendicular to \mathbf{b} , and s is a line element parallel to \mathbf{b} . Finally, γ is the Lorentz factor ($\gamma^2 = 1 / (1 - v^2/c^2) = c^2 / (c^2 - v^2)$). Using this factor, we define a relativistic parallel velocity $u_{\parallel} (= \gamma v_{\parallel})$ for simplicity of notation.

In order to make Eqs. (1) dimensionless, we define model dimensions using a field strength b_{scl} , lengthscale l_{scl} and timescale t_{scl} . Dimensionless quantities are related to their dimensional

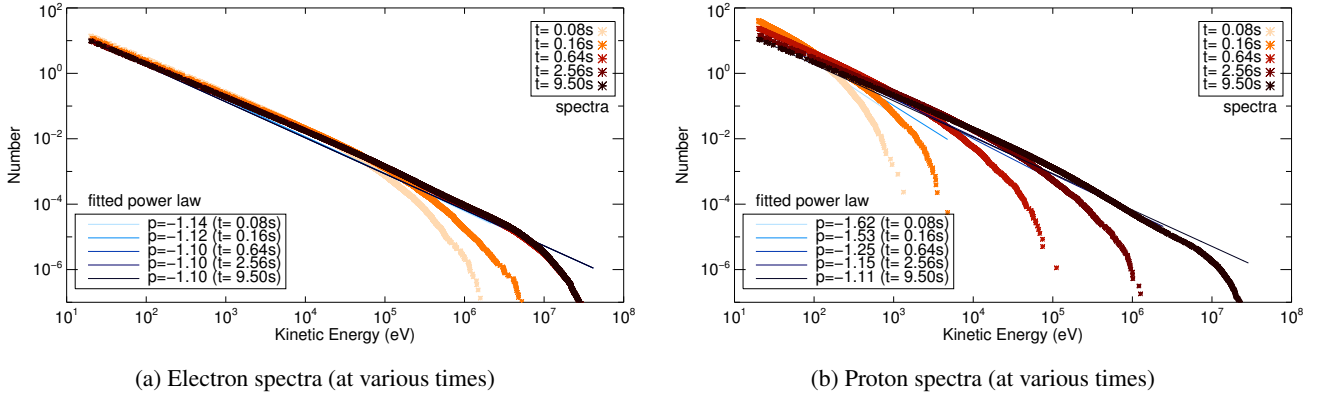


Fig. 4: Time evolution of energy spectra. Empirical probability distribution functions (and fitted power laws) for 2000 (a) electron and (b) proton energies recorded at various times throughout the orbit lifetimes (for key to times and fitted power laws, see legend). All particles had an initial energy of 20 eV, and were evenly distributed throughout the simulation domain (see e.g. Fig. 2a).

equivalent through:

$$\mathbf{B} = b_{scl} \bar{\mathbf{B}}, \quad x = l_{scl} \bar{x}, \quad t = t_{scl} \bar{t},$$

where the barred quantities represent dimensionless counterparts of the relevant variables. The choice of these quantities fixes the remaining normalising constants; for example, velocities in the model are scaled by $v_{scl}(= l_{scl} t_{scl}^{-1})$, energies by $KE_{scl}(= 0.5 m v_{scl}^2)$ and (assessing the dimensions of Faraday's Law) electric fields are scaled by $e_{scl}(= b_{scl} l_{scl} t_{scl}^{-1} = b_{scl} v_{scl})$. This investigation is motivated by the behaviour of particles in a solar coronal environment. We therefore fix our normalising parameters accordingly; unless otherwise stated, all experiments take $b_{scl} = 0.001$ T, $l_{scl} = 100$ km and $t_{scl} = 10$ s.

In order to further simplify Eqs. (1), only electrons or protons are considered here; this fixes the rest mass $m_0 = m_e = 9.1 \times 10^{-31}$ kg and charge $q = e = -1.6022 \times 10^{-19}$ C for electrons, or $m_0 = m_p = 1.67 \times 10^{-27}$ kg and $q = |e| = 1.6022 \times 10^{-19}$ C for protons. In this way, several normalising constants are expressed in terms of a normalising electron/proton gyro-frequency, $\Omega_{scl}(= q b_{scl} m_0^{-1})$. The factor of $\Omega_{scl} l_{scl}$ controls the scales at which certain guiding centre drifts become important.

Finally, several quantities in Eqs. (1) now also depend on the ratio of perpendicular electric field (E_{\perp}) to the magnitude of the magnetic field (B); for a given quantity X (representing either E or B), X^* and X^{**} are defined as

$$X^* = X \left(1 - \frac{1}{c^2} \frac{E_{\perp}^2}{B^2} \right)^{\frac{1}{2}}, \quad X^{**} = X \left(1 - \frac{1}{c^2} \frac{E_{\perp}^2}{B^2} \right).$$

These multiplying quantities are dimensionless, i.e. X^* and X^{**} retain the dimensions of X .

We evolve each of Eqs. (1) in time using a 4th order Runge-Kutta scheme with a variable timestep, subject to the numerically derived values of electric and magnetic fields found in a single snapshot of the MHD simulations of Bourdin et al. (2013) (discussed in Section 2.1). A similar approach has been used

by, for example Gordovskyy & Browning (2011); Gordovskyy et al. (2014). Each orbit is also terminated after the normalising timescale is reached, i.e. after 10 s of real time. The MHD simulation timescale is determined by the cadence of the observed magnetogram timeseries used to drive the photospheric boundary, which (for the results reported in Bourdin et al. 2013) is 90 s. By comparing the time between MHD snapshots and the timescale used in the guiding centre approximation code, we note that these scales are well separated. We also assume that the spatial scales of the gyro-motion and the global MHD environment are similarly separated, and will test this assumption for all orbits (see Sect. 3).

3. Global behaviour characteristics

We begin by studying the particle orbit behaviour for a uniform grid of initial positions spread throughout the computational domain in the horizontal direction at several different heights. Our aim is to obtain an overview of the global orbit behaviour one might typically expect to find throughout the AR.

For this investigation, an identical number of particles for each species were studied; 2000 electron orbits and 2000 proton orbits with an initial pitch angle of 45° and an initial kinetic energy of 20 eV. These choices are motivated by the findings of previous work (Threlfall et al. 2015), where it was shown that (if present) the contributions from any local parallel electric fields typically outweigh the choice of initial kinetic energy and pitch angle in impacting particle behaviour. Furthermore, while the initial kinetic energy chosen here is relatively low compared to the equivalent thermal energy ($20 \text{ eV} \approx 0.23 \text{ MK}$), this simply serves to aid illustration of particle orbit behaviour. We have also checked that a tenfold increase in initial particle energy does not significantly alter the overall findings reported here. Our particles are distributed in a $20 \times 20 \times 5$ grid in (x, y, z) ; the grid is evenly spaced and extends from $x, y \in [10, 200]$ Mm in five z -planes, at $z = [60, 65, 70, 75, 80]$ Mm above the photosphere. A visual

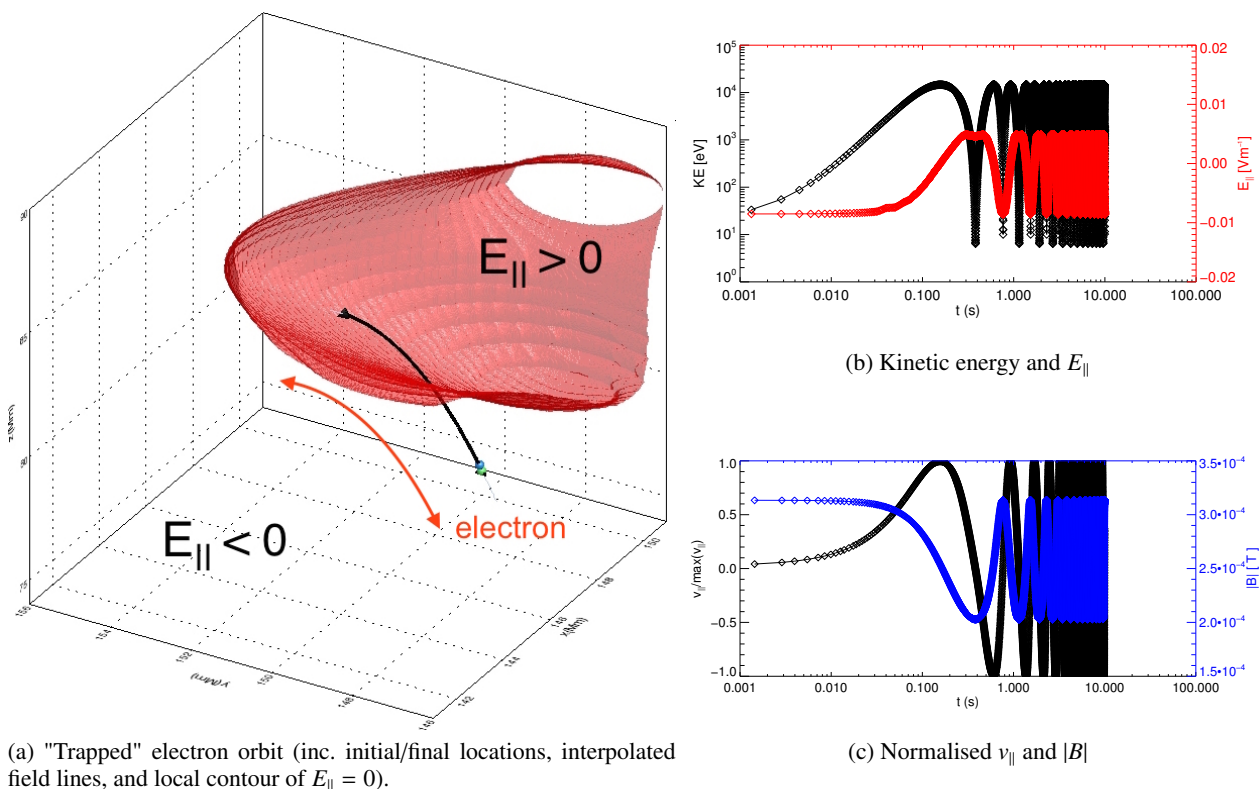


Fig. 5: Position A: example of electron which becomes "trapped". (a) displays a zoomed view of the electron orbit (thick black line), which begins at the location shown by a green orb, and ends at the location shown by the blue orb, while black trapezoids indicate locations where the parallel velocity of the particle changes sign. The thin grey line indicates the locally interpolated B -field line based on the initial position. The red isosurface denotes where the parallel electric field changes sign ($E_{\parallel} = 0$). Orbit properties for this electron are displayed in (b) and (c); (b) shows the change in kinetic energy (KE) and parallel electric field component (E_{\parallel}) as a function of time, while (c) shows the normalised parallel velocity ($v_{\parallel}/\max(v_{\parallel})$) and magnetic field strength ($|B|$) for this orbit.

representation of this grid is shown in Fig. 2a. This distribution of initial conditions of particle orbits was chosen to establish particle behaviour in a region encompassing the main AR features (including examples of both open and closed field structures), at large enough heights that both chromospheric effects (such as collisionality and partial ionisation) and numerical effects (primarily the inclusion of a stretched grid in z close to the photospheric boundary) could be minimised. Figure 3 shows the results of both the electron and proton orbit calculations for this distribution of initial conditions.

We will now highlight some key findings illustrated by Fig. 3. Firstly, all orbits (both protons and electrons) are accelerated to some degree, almost always due to the local parallel electric field. The majority of orbits achieve at least keV energies; the vast majority are accelerated to energies of 50-500 keV. By comparing Fig. 3a with Fig. 3b, it is clear that a similar number of electron and proton orbits achieve \gtrsim MeV energies. All of the orbits which achieve the highest energy levels in the survey have trajectories which head towards the lower solar atmosphere. Additionally, more electron than proton orbits may be found at the lowest energy levels. It is also apparent that several orbits, both proton and electron, appear to be continually reflected between mirror points; we will label these as "trapped" orbits.

The maximum kinetic energy of any orbit was achieved by an electron, whose kinetic energy reached 41.5 MeV (the highest energy reached by a proton was 28.7 MeV). The minimum kinetic energy was achieved by an electron, which gained 0.09 eV (the lowest energy gained by a proton was 0.5 eV). Regarding the question of scale separation, the maximum electron gyro-radius recorded was 0.41 m, while the maximum proton gyro-radius achieved during any orbit in the survey was 16.2 m. The x/y grid-point resolution of the MHD simulation is always 230 km; the resolution in the z -direction varies between 100 and 800 km (due to a non-equidistant grid). By comparison with the largest gyro-radii recorded, we can state that, at least in the case of the initial survey, the length scales of the MHD simulation and the particle orbits are sufficiently separate that our use of the guiding centre approximation is clearly justified.

For comparison with previous studies of particle acceleration, we briefly focus on the energy spectra created by this set of test-particle calculations. Figure 4 shows how the energy spectra of this initial distribution of protons and electrons behaves over time, for energies that reach at least 105% of their initial energy (focussing on accelerated particles). If a particle leaves the MHD simulation domain at any point, we record the final energy of the particle upon leaving the domain in any spectra at later times. A power law is also fitted to these spectra using the method of

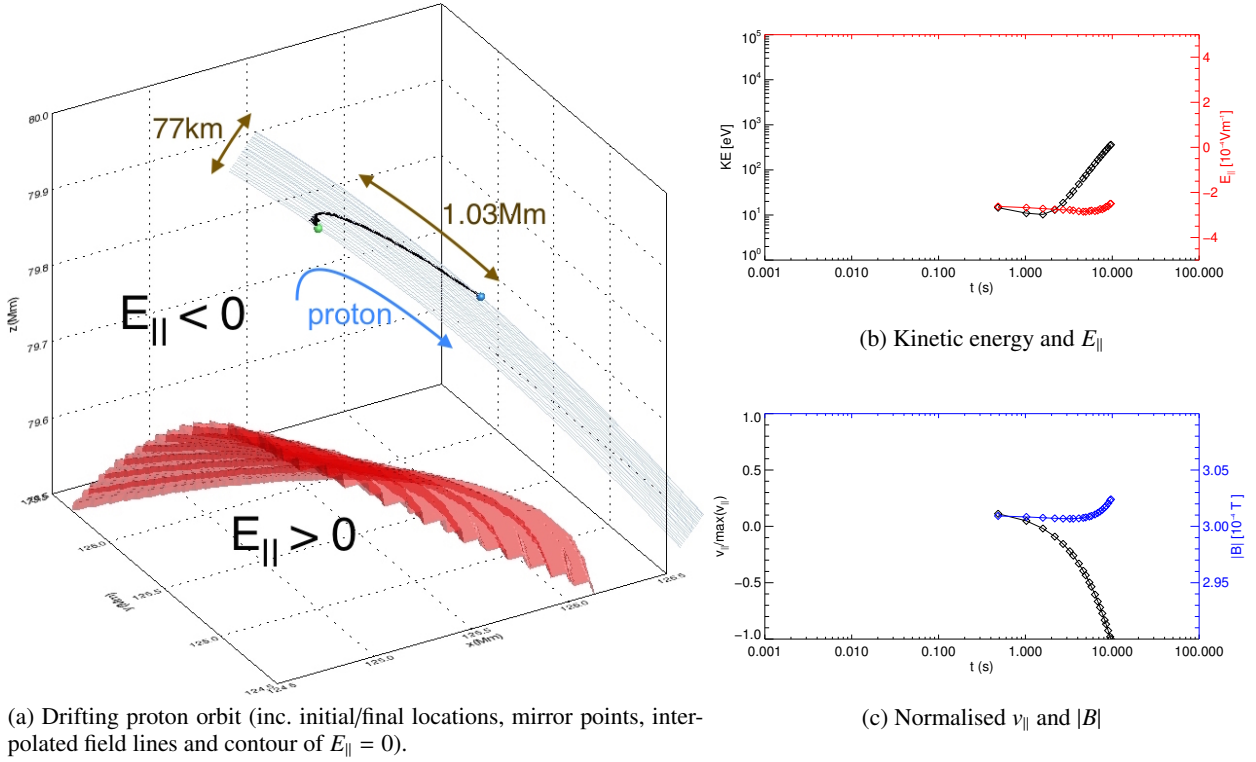


Fig. 6: Position B: example of proton which exhibits a slow guiding centre drift. (a) displays a zoomed view of the proton orbit (black), which begins at the location shown by a green orb, and ends at the location shown by a blue orb, with black trapezoids indicating the location of a change in sign of parallel velocity. The thin grey lines indicate locally interpolated B -field lines based on several orbit positions. The red isosurface denotes where the parallel electric field changes sign ($E_{\parallel} = 0$). Orbit properties for this proton are displayed in (b) and (c); (b) shows the change in kinetic energy (KE) and parallel electric field component (E_{\parallel}) as a function of time, while (c) shows the normalised parallel velocity ($v_{\parallel}/\max(v_{\parallel})$) and magnetic field strength ($|B|$) for this orbit.

maximum likelihood, (see e.g. Feigelson & Babu 2012). The resulting probability distribution function takes the form of

$$f_{\text{pow}}(E_k; p) = \frac{-(p+1)}{E_k^0} \left(\frac{E_k}{E_k^0} \right)^p, \quad E_k \geq E_k^0,$$

where E_k^0 is the minimum value of the kinetic energy E_k ($E_k^0 = 20$ eV here), and p is the power-law index. As with Threlfall et al. (2015), the spectra develop relatively hard power-law tails; approximately 90% of particles gain at least 1 keV in energy over the course of the orbit. While the power law is a relatively poor fit at early times (particularly in the proton case, Fig. 4b), we note that over time $p \rightarrow -1.11$ for both electrons and protons. Comparing Fig. 4a and Fig. 4b reveals that the high-energy tail is generated much more rapidly for electrons than protons (due to the difference in electron/proton mass). These spectra demonstrate the capability of this MHD environment to accelerate both protons and electrons upto several MeV, despite the lack of flaring activity.

In order to investigate the reasons behind the range of energies recovered and particle behaviour seen in this single AR system, we will now focus on several examples of individual particle orbit behaviour.

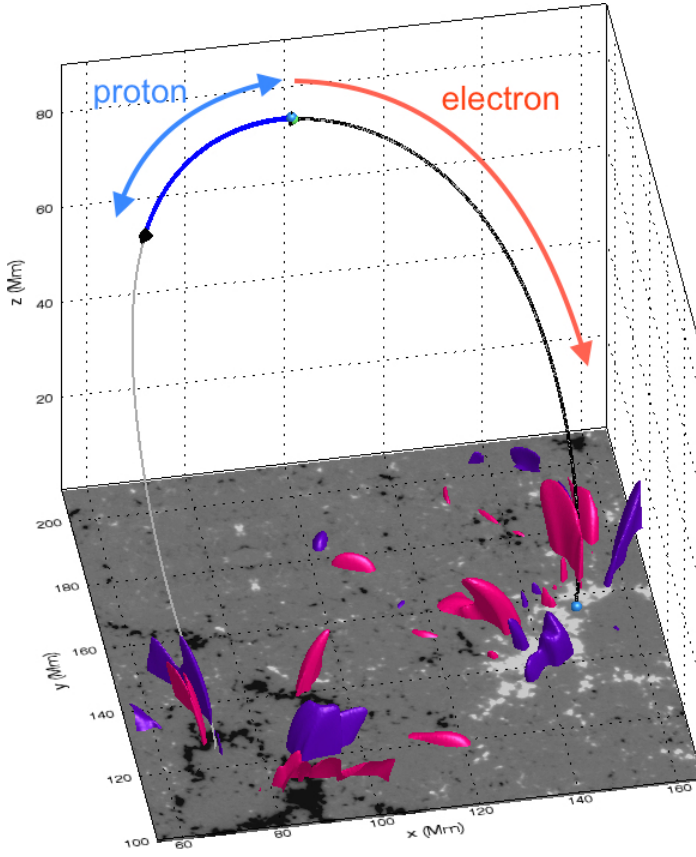
4. Examples of orbit behaviour encountered

A fairly broad range of behaviour was recovered in our initial survey of orbit behaviour, detailed in Section 3. We will now study three individual particle orbits whose initial positions are highlighted in Fig. 2; the examples selected illustrate three different types of characteristic particle behaviour observed in the simulations, which are discussed in detail below.

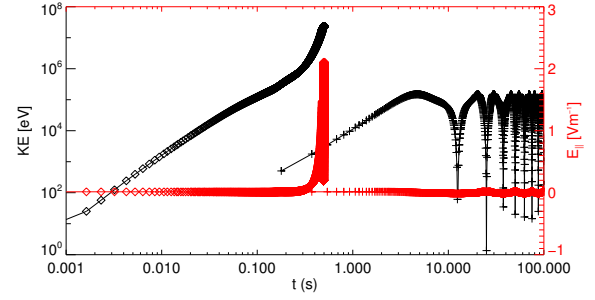
4.1. Trapped electrons

We begin with the particle labelled "A" in Fig. 2b. This is one of many electrons which are accelerated to large, but not extreme, energies over the course of the simulation. This orbit also remains within the coronal region of the AR core throughout the orbit lifetime, as with many of the particles seen in Fig. 3. For reference, the specific electron orbit we discuss is initially located at the centre of the grid, at position $(x, y, z) = (150, 150, 75)$ Mm, and remains trapped in the immediate vicinity of this position for the duration of the calculation (10 s), achieving a maximum kinetic energy of 14 keV in that time.

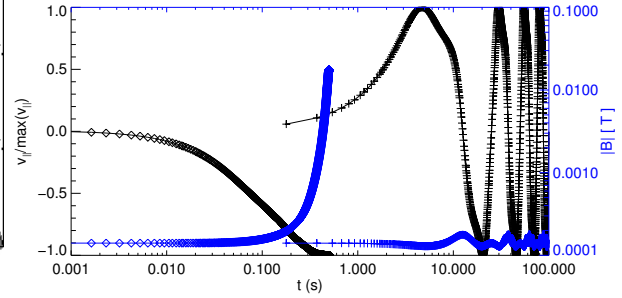
In Fig. 5, we present a close-up view of this specific orbit during this time, together with a study of the local conditions (determined by the MHD simulation) encountered by the particle over the course of the orbit. From Fig. 5a, it is clear that



(a) Accelerated proton & electron orbits, initial/final locations, interpolated field lines, regions of strong E_{\parallel} and photospheric magnetogram data.



(b) Kinetic energy and E_{\parallel}



(c) Normalised v_{\parallel} and $|B|$

Fig. 7: Position C: example of strong proton and electron acceleration. (a) displays a zoomed view of the proton (blue) and electron (black) orbits, which both begin at the location shown by a green orb, ending at a location(s) shown by a blue orb, and with changes in sign of v_{\parallel} indicated by black trapezoids. The thin grey lines indicate locally interpolated B -field lines based on the initial position, while contours of strong positive/negative E_{\parallel} , and the photospheric magnetogram of vertical magnetic field strength are included for context (see Fig. 2). Orbit properties for the electron and proton are displayed in (b) and (c) as diamonds (electron) and plus-signs (proton); (b) shows the change in kinetic energy (KE) and parallel electric field component (E_{\parallel}) as a function of time, while (c) shows the normalised parallel velocity ($v_{\parallel}/\max(v_{\parallel})$) and magnetic field strength ($|B|$) for each orbit.

the particle is trapped between mirror points (locations where the local parallel particle velocity reverses sign). One common cause of particle trapping is the *magnetic mirror effect* (where regions of increasing magnetic field strength cause the particle to reverse direction due to the adiabatic invariance of the magnetic moment, μ). In order to establish the role played by the magnetic mirror effect in this particular case, we study both the local parallel velocity and encountered magnetic field strength, in Fig. 5c, which suggests that changes in sign of v_{\parallel} are not strongly associated with locations of large peaks of $|B|$. To further clarify the role of the magnetic mirror effect, we calculate the loss cone angle for this position. Particles with pitch angle θ are naturally trapped by the magnetic mirror effect (in a so-called ‘magnetic bottle’) if

$$\sin(\theta) > \sqrt{\frac{B}{B_M}},$$

where B_M is the maximum magnetic field strength achieved at any location along a given field line; particles which escape this

magnetic trap (i.e. those with pitch angles which do not satisfy the above inequality) are said to be in the ‘loss cone’. The field line orbited by this electron (represented in Fig. 5b by a thin grey line) is actually a closed field line, anchored in the photosphere at both ends. We estimate the peak magnetic field strength at one foot-point to be 137 G, and 558 G at the other; these are the locations of greatest magnetic field strength at any point along this single field line (which are of course of opposite sign in the vertical direction at the photosphere). Thus, to be in the loss cone for this particular field line, a particle must have a pitch angle $\theta < 8.68^\circ$ in one direction and $\theta < 4.30^\circ$ in the other. We repeated the orbit calculation for an electron with the same initial position, but with a reduced initial pitch angle of $\theta = 4.0^\circ$; this now would ordinarily be sufficient for the particle to escape the natural magnetic trap caused by increasing magnetic field strength near the field-line foot-points. The orbit yielded by this second calculation was almost identical to that with $\theta = 45^\circ$; the particle remains trapped regardless of initial pitch angle. We can therefore exclude magnetic mirroring as the cause of this

type of electron trapping. This naturally leads to a question; if the electrons are not magnetically trapped, then how are they trapped?

The answer lies in the variation of the local electric field. For this electron, the orbit path encounters a change in the sign of the local parallel electric field, E_{\parallel} , as shown by the red curve in Fig. 5b. An iso-surface of the contour for which $E_{\parallel} = 0$ can be seen in Fig. 5a; the electron repeatedly crosses this contour over the course of its orbit.

Upon crossing the contour of $E_{\parallel} = 0$, the electron begins to decelerate. At the time when the local parallel velocity is approximately zero, the parallel electric field strength peaks; the orbit reverses direction (parallel to the magnetic field), re-crosses the $E_{\parallel} = 0$ contour and re-enters the region of oppositely signed E_{\parallel} , leading to further (and repeated) mirroring. This pattern repeats for the entire duration of the orbit simulation. This is not an isolated example; the vast majority of electrons which do not encounter the simulation boundaries are typically "trapped" this way. This trap is particularly effective for electrons. Even relatively weak regions of oppositely signed parallel electric field strength are sufficient to repeatedly accelerate electrons this way. By comparison, protons are much heavier; for a proton to be trapped in this manner requires both extreme and prolonged changes in the local value of E_{\parallel} in order for the proton to be decelerated sufficiently to reverse direction. Figure 3b shows that a large number of protons are also trapped, and hence are retained close to the centre of the AR core. This is unsurprising, due to the size and extent of the E_{\parallel} regions near the footpoints of field-lines which thread the AR core shown in Fig. 2b. An example of a proton which is trapped in this manner will be studied in more detail in Sect. 4.3.

4.2. Proton drifts

Turning our attention to protons, we now focus on another type of behaviour seen in the initial survey. Several proton orbits are also seen to only gain a relatively small amount of energy during the 10s calculation. One such orbit (labelled "B" in Fig. 2b) was initialised at $(x, y, z) = (125, 125, 80)$ Mm and gained (at its peak) 361 eV in kinetic energy. Once again we present a close-up view of the orbit path, together with local plasma conditions in Fig. 6.

It is clear from Fig. 6a that this proton experiences a relatively constant (anti-)parallel electric field strength throughout its lifetime; the orbit path remains distant from the contour representing $E_{\parallel} = 0$ (also shown by the value of E_{\parallel} in Fig. 6b). However, despite the lack of a change in sign of E_{\parallel} or a clear peak in $|B|$ (in Fig. 6c, which would potentially signal the magnetic mirror effect), a mirror point is clearly visible close to the point of initialisation (green orb), and in-between the initial and final particle positions (c.f. Fig. 5a, where the mirror points enclose the initial and final particle positions!). The mirror point

location may be understood by again considering local plasma conditions.

Having initialised the proton orbit with a positive parallel velocity (i.e. a velocity parallel to \mathbf{B}), the proton decelerates from its slow initialisation speed (due to the sign of the local parallel electric field). The large proton mass (compared to an electron) causes this deceleration to take place over a longer timescale (than that taken by an electron); during this time, particle drifts (primarily the $\mathbf{E} \times \mathbf{B}$ drift) begin to play a significant role in the proton trajectory.

Figure 6a includes interpolated magnetic field lines based on the changing position of the proton guiding centre over time. From this, it is clear that the proton no longer follows the same field line for all time, but instead drifts across many field lines¹, before finally beginning to accelerate in the opposite direction to the initial direction of travel. For this particular orbit, after 10 s, the perpendicular displacement of the proton from its original field line is approximately 77 km; by comparison, the final parallel displacement is 1.03 Mm (with a peak positive displacement along the field of approximately 31 km, before being accelerated in the opposite direction over a distance of 1.06 Mm). Over the course of the orbit, the proton experiences a near-constant $\mathbf{E} \times \mathbf{B}$ drift velocity of approximately 7.81 km/s; integrating this value over the 10 s orbit lifetime yields a perpendicular displacement which agrees with that observed in Fig. 6a. Furthermore, the perpendicular displacement is well-aligned with the local $\mathbf{E} \times \mathbf{B}$ vector. While the parallel displacement is likely to further increase with time and typically will dominate over perpendicular drifts (particularly for large values of E_{\parallel} or long timescales), this case demonstrates that proton orbits may in fact drift over relatively large distances, particularly upon encountering regions of deceleration.

4.3. Accelerated electrons/protons

Several examples of both the electron "trapping" and proton drifting can be observed in our survey. However, by far the most common type of behaviour present is that of strong direct acceleration (of both electrons and protons) due to the strength of the local parallel electric field. We will explore this class of behaviour by illustrating the orbits of both an electron and a proton which are both initialised in the same location (labelled "C" in Fig. 2b), and which (initially) encounter (the same) strong parallel electric fields. As with previous examples, we will illustrate a

¹ The $\mathbf{E} \times \mathbf{B}$ drift velocity can be effectively regarded as the kinetic equivalent of the MHD fluid velocity recovered in the simulations of the (macroscopic) environmental behaviour. The fact that the $\mathbf{E} \times \mathbf{B}$ drift is responsible for orbits crossing many field lines in a single snapshot may initially appear to suggest that the separation of MHD and kinetic scales no longer holds. However, the total distance drifted in the orbit simulations remains well below the spatial and temporal resolution of the MHD simulation. Thus, on an MHD level, the particle would orbit around a single field line which moves with the fluid velocity from snapshot to snapshot. However, using only a single MHD snapshot, this motion is instead seen as a drift across several (static) field lines.

close-up view of the orbit path and the local plasma parameters encountered, in Fig. 7. For reference, the initial position used in this example is $(x, y, z) = (100, 200, 80)$ Mm. To further emphasise the differences in behaviour between species, we extend the simulation time from 10 s to 100 s for this case. This extends the particle simulations beyond the cadence of the MHD simulations; in extending the simulation time in this manner, we simply aim to illustrate particle behaviour over a longer term.

In Fig. 7a, the initial position is located near the apex of a closed field line which links the foot-points of the AR studied. The proton (yellow orbit) and electron (black orbit) are accelerated towards opposing foot-points (as one might expect due to the charge difference between the species). Furthermore, while the electron is rapidly accelerated almost all the way to the photospheric boundary, the proton never leaves the (upper) corona, but is ultimately reflected and returning along the initial trajectory, before further repeated mirroring at later times.

In order to assess the reason for the proton becoming trapped, we once again calculate the loss cone (see discussion in Sect. 4.1 for more details). Along the field line in question, we estimate that initial pitch angles less than 5.81° and 6.61° would enable particles to escape the trap caused by increasing magnetic field strength. As with the case shown in Sect. 4.1, repeating this experiment with an initial pitch angle of 4.0° shows negligible differences in proton/electron behaviour; both the acceleration and trapping behaviour displayed in Fig. 7 are caused by the electric field. In extending the simulation time from 10 s to 100 s, we demonstrate that the electric field continues to trap the proton in the upper atmosphere for all time, while accelerating the electron until it reaches the loop foot-point at the photospheric boundary.

All particle orbit calculations are automatically terminated upon reaching a 5 Mm layer above the lower simulation boundary (due to the limited applicability of our test-particle approach in this region). At termination, the electron has travelled approximately 118 Mm in less than 0.5 s. By comparison, the distance between mirror points for the proton is approximately 38 Mm. The reason for the differences between the proton and electron results are twofold; from Fig. 7c, we can see that the proton achieves its peak velocity after approximately 4 – 5 s, taking much longer to accelerate. Upon encountering a region of oppositely oriented E_{\parallel} , the proton is unable to overcome the resulting deceleration, and mirrors. By comparison, the electron is continually accelerated as it plummets towards the photosphere; this continuing direct acceleration is sufficient to allow the electron to escape the "magnetic bottle" created by the loop foot-points.

5. Discussion

We have conducted a large survey of test-particle behaviour in an environment which aims to describe the behaviour of a solar AR. From this survey (detailed in Sect. 3), it is clear that this environment would cause a significant amount of particle accel-

eration to non-thermal energies. Both electron and proton spectra (Fig. 4) evolve high-energy power-law tails whose index is small, even for observed flaring events. While the power-law index at later times is in a range which is sometimes achieved by kinetic particle models (e.g. Baumann et al. 2013, who recover a power-law index of -1.78), our work is specifically focussed on a non-flaring AR. Lacking observational evidence of a flare in this region, our results suggest that even the latest advanced MHD models which purport to describe the behaviour of AR reconnection and heating are insufficient to model the physical processes seen in observations at the kinetic level. The acceleration found in our surveys of particle behaviour is entirely due to the strength and extent of regions of parallel electric field. While the level of Ohmic heating recovered by Bourdin et al. (2013) is shown to accurately relate to the locations and amount of heating observed in this AR, the size of the current sheets which form and the level of resistivity used in this (and similar) simulations generates large, broad electric fields, which (on a particle level) typically dominate other contributions to particle motion.

The strength and extent of these electric fields are clearly illustrated in Fig. 2. We estimate the peak parallel electric field in the simulation domain to be $E_{\parallel}^{\text{peak}} = 295$ V/m, while in the corona (i.e. above the lowest 10 gridpoints), $E_{\parallel}^{\text{peak}} \approx 5$ V/m. For comparison, we estimate the Dreicer electric field to approach 6×10^{-2} V/m (for $n = 1 \times 10^{16} \text{ m}^{-3}$, $T = 1$ MK). Thus the electric field strengths in the simulation are not only often super-Dreicer, but also can reach into the simulated corona (see e.g. Fig. 2b). In Threlfall et al. (2015), a magnetic reconnection experiment with $E_{\parallel}^{\text{peak}} \approx 0.1$ V/m was sufficient to rapidly accelerate large numbers of particles to non-thermal energies, despite the apparent strength appearing too small to be considered relevant for solar flares. In fact, both the electric field strength and the extent of the reconnection region (which, for some cases in Threlfall et al. 2015, reached 20 Mm) determine the reconnection rate and (ultimately) the energy gained by the particle through direct acceleration. Thus both the strength and extent of the electric fields in the work of Bourdin et al. (2013) are responsible for the non-thermal particle populations recovered here.

While many of the particles experience acceleration, several test-particle cases remain at relatively low (thermal) energies. In Sect. 4.1, we illustrate an electron which is "trapped" between weak regions of oppositely oriented parallel electric field. Such trapping has not previously been reported; recent examples of particle behaviour in different configurations (e.g. Gordovskyy et al. 2014; Threlfall et al. 2015) may not observe this type of trapping, if uni-directional electric field structures are formed during reconnection. However, for a general coronal structure containing reconnecting fragmented current-sheets and bi-polar magnetic fields, one might expect that particles of all energies are likely to encounter regions of oppositely oriented parallel electric field. While small weak parallel electric field regions would be able to trap electrons, we have also demonstrated that regions of strong, prolonged changes in E_{\parallel} might

also be able to trap protons (see Sect. 4.3). Whether or not this type of trapping would yield an observational signature (e.g. in radio wavelengths) is at present unknown, and may be worthy of further investigation. While trapped, these particles would also likely lose energy due to collisional effects, particularly lower down in the atmosphere, or at low speeds (e.g. during deceleration/reflection). We have also shown that, particularly for cases involving proton deceleration (in Sect. 4.2), particle drifts may in fact play a significant role in particle trajectories, where a proton may in fact drift upto (potentially) tens/hundreds of kilometres from its original field line. Such drifts may contribute to the lack of alignment in X-ray and γ -ray features observed during a single solar flare event (e.g. Hurford et al. 2003).

Finally, it is worth noting that, of the characteristic types of behaviour discussed in Sect. 4, two of these are likely to be critically affected by the choice of numerical resistivity used in the simulation. Reducing this value would weaken the strength of the electric fields generated, and reduce both the magnitude of the $E \times B$ drift velocity, and the voltage through which particles are accelerated, producing a smaller distribution of non-thermal particles. However, we would also anticipate that the trapping behaviour first seen in Sect. 4.1 would remain relatively unchanged. If the magnetic diffusivity (here adapted to the grid spacing) was smaller (as it would be in reality on the Sun) then reconnection would be held off for longer, leading to the generation of more localised current layers, which would be associated with strong local electric fields (greater than found in this simulation). However, outwith these localised current layers much weaker (approximately zero) electric fields would occur which may change sign frequently. Indeed, with larger regions of no parallel electric field, more particles (particularly electrons) are likely to find themselves mirroring between smaller weaker regions of oppositely oriented parallel electric field. Only by encountering regions of strong E_{\parallel} (and thus achieving high velocities) are these particles capable of passing through the trap set by these weak field regions.

6. Conclusions and future work

We have studied the relativistic guiding centre behaviour of test particles in an observationally driven large-scale 3D magnetic reconnection experiment (Bourdin et al. 2013).

We find that the majority of particle motion is controlled by the strength, orientation and extent of the local parallel electric field; in the vast majority of cases, the electric field causes strong direct acceleration of particles to non-thermal energies. In light of the lack of evidence for a flare-like event within this AR, our results imply that the resistivity and current structures created in the MHD simulation combine to produce electric fields which are higher and more extended than that required to produce a purely thermal particle population.

As part of this investigation, we have identified several behavioural characteristics of particles within this environ-

ment. Direct acceleration and drifting of particles were anticipated and would likely be weakened by simulations containing weaker/shorter electric field regions. However, we also observe a type of trapping of particles between regions of oppositely oriented parallel electric field which has not been seen before in studies of particle acceleration. This type of trap results from a change in sign of the parallel electric fields, and should be present in any test particle calculations based on compressible resistive MHD simulations of AR behaviour. Reducing the electric field strengths in the model may in fact allow more particles to become trapped by this mechanism (in the present survey, many are simply accelerated to non-thermal energies, thus avoiding the "trap"). Whether or not this type of trap would produce an observational signature is unknown, but if it does it could allow for further insights into electric field structures within the solar atmosphere.

Following on from the present investigation, several opportunities for further work present themselves. The work of Bourdin et al. (2013) merits repeating, particularly to see how the results presented here change for lower magnetic diffusivities. The use of observations to drive MHD simulations is important, and worthy of repeating for a more recent active-region system (including regions that produce or do not produce a flare) which can be observed by a full suite of modern instruments, e.g. RHESSI, AIA/SDO, STEREO and ground-based telescopes. This might also allow for a comparison of synthetic hard X-ray data (generated by test-particle simulations) and a specific flare-like event, in a similar manner to that used in Gordovskyy et al. (2014). Furthermore, development of the test-particle model (for example, by studying the effect of collisions, or through the use of a distribution function which better reflects the initial state of particles in a coronal environment) would also be beneficial.

Acknowledgements. The authors gratefully acknowledge the support of the U.K. Science and Technology Facilities Council [Consolidated Grant ST/K000950/1]. The research leading to these results has received funding from the European Commission's Seventh Framework Programme FP7 under the grant agreement SHOCK (project number 284515). This work was supported by the International Max-Planck Research School (IMPRS) on Solar System Physics. The results of this research have been achieved using the PRACE Research Infrastructure resource *Curie* based in France at TGCC, as well as *JuRoPA* hosted by the Jülich Supercomputing Centre in Germany. Preparatory work has been executed at the Kiepenheuer-Institut für Sonnenphysik in Freiburg, as well as on the bwGRiD facility located at the Universität Freiburg, Germany. We thank Suguru Kamio for his help finding active region observations. Hinode is a Japanese mission developed, launched, and operated by ISAS/JAXA, in partnership with NAOJ, NASA, and STFC (UK). Additional operational support is provided by ESA and NSC (Norway).

References

- Baumann, G., Haugbølle, T., & Nordlund, Å. 2013, *ApJ*, 771, 93
- Bourdin, P.-A., Bingert, S., & Peter, H. 2013, *A&A*, 555, A123
- Bourdin, P.-A., Bingert, S., & Peter, H. 2014a, *PASJ*, 66, 1
- Bourdin, P.-A., Bingert, S., & Peter, H. 2014b, *Cent. Eur. Astrophys. Bull.*, 38, 1
- Bourdin, P.-A., Bingert, S., & Peter, H. 2015, *A&A*, submitted
- Brandenburg, A. & Dobler, W. 2002, *Computer Physics Communications*, 147, 471
- Browning, P. K. & Vekstein, G. E. 2001, *J. Geophys. Res.*, 106, 18677
- Bruhwyler, D. L. & Zweibel, E. G. 1992, *J. Geophys. Res.*, 97, 10825

- Bulanov, S. V. & Sasorov, P. V. 1976, *Soviet Ast.*, 19, 464
- Cargill, P. J., Vlahos, L., Baumann, G., Drake, J. F., & Nordlund, Å. 2012, *Space Sci. Rev.*, 173, 223
- Cook, J. W., Cheng, C.-C., Jacobs, V. L., & Antiochos, S. K. 1989, *ApJ*, 338, 1176
- Culhane, J. L., Harra, L. K., James, A. M., et al. 2007, *Sol. Phys.*, 243, 19
- Dalla, S. & Browning, P. K. 2005, *A&A*, 436, 1103
- Dalla, S. & Browning, P. K. 2006, *ApJ*, 640, L99
- Dalla, S. & Browning, P. K. 2008, *A&A*, 491, 289
- Drake, J. F., Swisdak, M., Che, H., & Shay, M. A. 2006, *Nature*, 443, 553
- Eradat Oskoui, S. & Neukirch, T. 2014, *A&A*, 567, A131
- Eradat Oskoui, S., Neukirch, T., & Grady, K. J. 2014, *A&A*, 563, A73
- Feigelson, E. & Babu, G. 2012, *Modern Statistical Methods for Astronomy: With R Applications* (Cambridge University Press), 90
- Fletcher, L., Dennis, B. R., Hudson, H. S., et al. 2011, *Space Sci. Rev.*, 159, 19
- Golub, L., Deluca, E., Austin, G., et al. 2007, *Sol. Phys.*, 243, 63
- Gordovskyy, M. & Browning, P. K. 2011, *ApJ*, 729, 101
- Gordovskyy, M., Browning, P. K., Kontar, E. P., & Bian, N. H. 2014, *A&A*, 561, A72
- Gordovskyy, M., Browning, P. K., & Vekstein, G. E. 2010, *ApJ*, 720, 1603
- Grady, K. J. & Neukirch, T. 2009, *A&A*, 508, 1461
- Grady, K. J., Neukirch, T., & Giuliani, P. 2012, *A&A*, 546, A85
- Gudiksen, B. V. & Nordlund, Å. 2005a, *ApJ*, 618, 1031
- Gudiksen, B. V. & Nordlund, Å. 2005b, *ApJ*, 618, 1020
- Guo, J.-N., Büchner, J., Otto, A., et al. 2010, *A&A*, 513, A73
- Hannah, I. G. & Fletcher, L. 2006, *Sol. Phys.*, 236, 59
- Hannah, I. G., Hudson, H. S., Battaglia, M., et al. 2011, *Space Sci. Rev.*, 159, 263
- Hesse, M. & Schindler, K. 1988, *J. Geophys. Res.*, 93, 5559
- Hurford, G. J., Schwartz, R. A., Krucker, S., et al. 2003, *ApJ*, 595, L77
- Kliem, B. 1994, *ApJS*, 90, 719
- Kosugi, T., Matsuzaki, K., Sakao, T., et al. 2007, *Sol. Phys.*, 243, 3
- Lin, R. P., Dennis, B. R., Hurford, G. J., et al. 2002, *Sol. Phys.*, 210, 3
- Litvinenko, Y. E. 1996, *ApJ*, 462, 997
- Northrop, T. 1963, *The adiabatic motion of charged particles*, Interscience tracts on physics and astronomy (Interscience Publishers)
- Onofri, M., Isliker, H., & Vlahos, L. 2006, *Physical Review Letters*, 96, 151102
- Parker, E. N. 1972, *ApJ*, 174, 499
- Parnell, C. E. & De Moortel, I. 2012, *Royal Society of London Philosophical Transactions Series A*, 370, 3217
- Parnell, C. E., Stevenson, J. E. H., Threlfall, J., & Edwards, S. J. 2015, *Royal Society of London Philosophical Transactions Series A*
- Schindler, K., Hesse, M., & Birn, J. 1988, *J. Geophys. Res.*, 93, 5547
- Schindler, K., Hesse, M., & Birn, J. 1991, *ApJ*, 380, 293
- Spitzer, L. 1962, *Physics of Fully Ionized Gases*
- Stanier, A., Browning, P., & Dalla, S. 2012, *A&A*, 542, A47
- Testa, P., De Pontieu, B., Allred, J., et al. 2014, *Science*, 346, B315
- Threlfall, J., Neukirch, T., Parnell, C. E., & Eradat Oskoui, S. 2015, *A&A*, 574, A7
- Turkmani, R., Vlahos, L., Galsgaard, K., Cargill, P. J., & Isliker, H. 2005, *ApJ*, 620, L59
- Vandervoort, P. O. 1960, *Annals of Physics*, 10, 401
- Vilmer, N., MacKinnon, A. L., & Hurford, G. J. 2011, *Space Sci. Rev.*, 159, 167
- Wood, P. & Neukirch, T. 2005, *Sol. Phys.*, 226, 73
- Zharkova, V. V., Arzner, K., Benz, A. O., et al. 2011, *Space Sci. Rev.*, 159, 357
- Zharkova, V. V. & Gordovskyy, M. 2004, *ApJ*, 604, 884
- Zharkova, V. V. & Gordovskyy, M. 2005, *MNRAS*, 356, 1107